



## Morphology-driven automatic segmentation of MR images of the neonatal brain

Laura Gui<sup>a,\*</sup>, Radoslaw Lisowski<sup>a,b</sup>, Tamara Faundez<sup>a</sup>, Petra S. Hüppi<sup>a</sup>, François Lazeyras<sup>b</sup>, Michel Kocher<sup>c</sup>

<sup>a</sup> Division of Development and Growth, Department of Pediatrics, University of Geneva, Geneva, Switzerland

<sup>b</sup> Department of Radiology and Medical Informatics, University of Geneva, Switzerland

<sup>c</sup> Biomedical Imaging Group, Ecole Polytechnique Fédérale de Lausanne, Lausanne, Switzerland

### ARTICLE INFO

#### Article history:

Received 6 April 2012

Received in revised form 6 July 2012

Accepted 16 July 2012

Available online 31 July 2012

#### Keywords:

Automatic segmentation  
Magnetic resonance imaging  
Neonatal brain  
Watershed segmentation  
Mathematical morphology

### ABSTRACT

The segmentation of MR images of the neonatal brain is an essential step in the study and evaluation of infant brain development. State-of-the-art methods for adult brain MRI segmentation are not applicable to the neonatal brain, due to large differences in structure and tissue properties between newborn and adult brains. Existing newborn brain MRI segmentation methods either rely on manual interaction or require the use of atlases or templates, which unavoidably introduces a bias of the results towards the population that was used to derive the atlases. We propose a different approach for the segmentation of neonatal brain MRI, based on the infusion of high-level brain morphology knowledge, regarding relative tissue location, connectivity and structure. Our method does not require manual interaction, or the use of an atlas, and the generality of its priors makes it applicable to different neonatal populations, while avoiding atlas-related bias. The proposed algorithm segments the brain both globally (intracranial cavity, cerebellum, brainstem and the two hemispheres) and at tissue level (cortical and subcortical gray matter, myelinated and unmyelinated white matter, and cerebrospinal fluid). We validate our algorithm through visual inspection by medical experts, as well as by quantitative comparisons that demonstrate good agreement with expert manual segmentations. The algorithm's robustness is verified by testing on variable quality images acquired on different machines, and on subjects with variable anatomy (enlarged ventricles, preterm- vs. term-born).

© 2012 Elsevier B.V. All rights reserved.

### 1. Introduction

The neonatal period is a critical time in brain development. Its investigation is not only scientifically important, but also indispensable in the elaboration of preventive methods and treatments for infants at risk (Hüppi et al., 1998, Cachia et al., 2003). The segmentation of neonatal brain MRI is a primary component in the study of neonatal brain development, opening the way towards analyses of tissue volumetry, cortical folding, cortical parcellation and connectivity (Hüppi et al., 1998, Cachia et al., 2003).

The aim of brain segmentation is to delineate both large-scale brain areas, such as the cerebellum, the brainstem and the two hemispheres, and small-scale structures (tissues), such as the gray matter, the white matter, and the cerebrospinal fluid (CSF). In addition to these tissues, in the case of newborns we are also interested in distinguishing between cortical and subcortical gray matter, and between myelinated and unmyelinated white matter, which is cru-

cial in the evaluation of the white matter myelination process – an indicator of brain maturation.

The segmentation of newborn brain MRI poses additional challenges compared to the segmentation of adult MRI. These are first of all due to the different properties and quality of the input images in the two cases. In order to capture the smaller sized structures of the newborn brain, higher resolution images need to be acquired during limited periods (to avoid artifacts due to infant motion), leading to lower signal-to-noise ratios and to stronger partial volume effects. Furthermore, since the water content of white matter (mostly unmyelinated at birth) is close to that of the gray matter, the gray-white matter contrast is inverted and significantly reduced compared to adult MRI, leading to lower contrast-to-noise ratios. To overcome this problem, T2 images are acquired in addition to the T1 images, offering better gray-white matter contrast. Moreover, the contrast inversion in the newborn images worsens the partial volume problem at the interface between gray matter and CSF. Since the average intensity of the two tissues coincides with the intensity of unmyelinated white matter, voxels at their interface are misclassified as unmyelinated white matter by an intensity-only classification. An additional difficulty for the segmentation of the newborn brain is posed by the ongoing white matter myelination process, which proceeds gradually through

\* Corresponding author. Address: Center for Biomedical Imaging (CIBM), Department of Radiology, Geneva University Hospitals (HUG), Rue Gabrielle-Perret-Gentil 4, Geneva, Switzerland. Tel.: +41 22 37 25 216; fax: +41 22 37 27 072.

E-mail address: [Laura.Gui@unige.ch](mailto:Laura.Gui@unige.ch) (L. Gui).

the brain and makes the intensities of white matter similar to those of gray matter in both T1 and T2 images.

A large amount of work has been dedicated to the segmentation of adult brain MRI, resulting in many successful approaches, some of which are available as freely distributed software (Suri et al., 2002; Fischl et al., 2002; Cocosco et al., 2003; Grau et al., 2004; Ashburner and Friston, 2005, and references therein). Due to large differences in brain structure between the newborn and the adult, these methods cannot be used to segment the newborn brain and dedicated methods need to be developed. Over the past years we have seen important advances in newborn brain MRI segmentation, prompted by an increase in the quality and availability of neonatal imagery.

Many authors used manual voxel selection or manual segmentation of training images in order to derive image intensity models for the tissues targeted for segmentation. In particular, manual selection was used to obtain training data for  $k$ -nearest neighbors (KNN) classification schemes integrating intensity data and spatial priors given by templates (Warfield et al., 2000) or training voxel coordinates (Anbeek et al., 2008). Weisenfeld et al. (2006) refined the algorithm of Warfield et al. (2000) by combining KNN tissue intensity density estimation with probabilistic tissue atlas priors and a Markov random field (MRF) prior imposing spatial homogeneity. Their method was extended by Weisenfeld and Warfield (2009), who developed a library of template subjects with manually-selected tissue class prototypes. Their algorithm learns tissue class probabilities in the target subject from training data obtained by template alignment and prototype projection to the target subject. This generates a set of automatic segmentations of the target subject, one for each template subject, which are fused into a consensus segmentation via an expectation-maximization (EM) scheme. The segmentation is refined by pruning out inconsistent prototypes, and then reiterating the process. In the context of an MRF image model segmented via graph-cuts, Song et al. (2007) also resorted to manual segmentations to derive a Parzen-windows intensity model, and to train an image intensity classifier consisting of Support Vector Machines (SVMs).

An alternative to manual selection for obtaining tissue intensity models is the use of unsupervised learning techniques, often implemented via EM schemes, where tissue intensity model estimation is interleaved with voxel classification in an iterative process, frequently guided by probabilistic atlas priors and MRF priors enforcing spatial homogeneity. Such EM schemes are the foundation of classic methods for the segmentation of adult brains (Leemput et al., 1999b; Ashburner and Friston, 2005), and were adopted and enhanced by several authors in order to deal with the specific problems of neonatal brain segmentation. For instance, Prastawa et al. (2005) employed robust graph clustering (Cocosco et al., 2003) to separate myelinated from unmyelinated white matter, and to prune tissue intensity samples used in nonparametric density estimation. Xue et al. (2007) were the first ones who specifically addressed the problem of misclassified partial volume voxels at the gray matter/CSF interface by augmenting the classic EM-MRF scheme with a partial-volume removal step. Bach-Cuadra et al. (2009) segmented the fetal brain by EM-fitting of a Gaussian mixture model, refined via an MRF model imposing spatial and anatomical priors. Habas et al. (2010) created an atlas of the fetal brain and applied it as a prior in an EM scheme similar to Leemput et al. (1999b) in order to segment the fetal brain. Shi et al. (2010) used segmentations of better-contrasted later-age scans of their subjects' brains (at one or two years of age) as priors for the segmentation of their corresponding neonatal scans. In the absence of longitudinal data, the same authors (Shi et al., 2011a) employed a neonatal brain atlas constructed by weighting subjects previously segmented (Shi et al., 2010) based on their similarity to the current segmentation subject. Yu et al. (2010) combined manual

segmentation of weakly contrasted subcortical structures, brainstem and cerebellum with automatic segmentation of gray matter, white matter and CSF via an EM scheme similar to Leemput et al. (1999b).

While most of the above authors used their own templates and atlases to guide segmentation, recently several authors have developed and published specific brain atlases to help the segmentation and study of the neonatal brain (Kuklisova-Murgasova et al., 2011; Oishi et al., 2011; Shi et al., 2011b). In particular, the atlas of Shi et al. (2011b) was used by Wang et al. (2011) to segment the neonatal brain via a coupled level-set method incorporating a thickness constraint on the cortical region. Coupled surface evolution was also employed by Leroy et al. (2011) to determine the gray-white matter interface, in an atlas-free approach driven by local image contrast and geometrical features.

In order to cope with the challenges of neonatal brain segmentation, most of the above-mentioned authors introduced strong prior knowledge into the segmentation schemes, in the form of probabilistic atlases, templates or manually selected prototypes. In addition to manual intervention being time-consuming, all these forms of prior knowledge are highly dependent on the population that they were obtained from, and therefore are not necessarily suitable for different populations. For instance, an atlas obtained from term-born neonates is not suitable for the segmentation of premature-born neonates scanned at term, due to considerable differences in brain shape and structure between the two populations (Inder et al., 2005; Kapellou et al., 2006). Moreover, segmentation results are often used to investigate structural brain differences between different groups (for instance, in relation to the administration of different drugs). In such a case, the application of atlas prior information comes with the risk of eliminating population differences that would otherwise be reflected by the segmentation. Finally, the use of an atlas as segmentation prior relies on its successful registration to the target brain, which is challenging, especially in high-variability regions such as the cortex.

In this paper, we propose a different approach to neonatal brain segmentation, based on the use of general, widely-accepted knowledge of neonatal brain morphology, integrating information about tissue connectivity, structure and relative positions. For instance, we use the information that the white matter is a connected tissue, surrounded by cortical gray matter, which in turn is surrounded by extra-ventricular CSF. This information is conveyed in the form of neighborhood selection criteria for a region growing algorithm separating white matter, gray matter and CSF, where we avoid partial volume errors at the gray matter/CSF interface by imposing the condition that the white matter cannot grow in the neighborhood of extra-ventricular CSF. Similarly, each step of our algorithm is based on fundamental, well-established segmentation techniques (such as the marker-based watershed segmentation and region-based active contours, see e.g. Beucher and Meyer, 1993; Grau et al., 2004; Cousty et al., 2010; Chan and Vese, 2001; Osher and Paragios, 2003), where we apply specifically designed segmentation functions encapsulating high-level brain morphology knowledge. In contrast to atlas-based methods, the use of such high-level morphological information ensures our method's generality and widespread applicability to different populations of newborn brains. To our knowledge, up to date there are only two other methods which do not employ neither atlas priors, nor manual intervention: Bach-Cuadra et al. (2009), who segment the fetal brain into white matter, cortical and subcortical gray matter and CSF, and Leroy et al. (2011), who segment the gray-to-white matter interface of infants from one to 4 months of age. The proposed algorithm is able to perform a comprehensive segmentation of the newborn brain, distinguishing both large-scale structures, namely the two hemispheres, the cerebellum and the brainstem, and fine-scale structures, namely the cortical and the subcortical

gray matter, the myelinated and the unmyelinated white matter and the CSF. The automatic segmentation of the two brain hemispheres is an important step towards outlining their functional and morphological differences, which are distinguishable at an early age (Dubois et al., 2010). Moreover, segmentations of the cerebellum and brainstem are necessary in the assessment of brain maturation and eventual disfunction (Hüppi et al., 1998). The same is true for the segmentation of the cortical and subcortical gray matter, and of the myelinated and unmyelinated white matter (Weisenfeld and Warfield, 2009). To our knowledge, the proposed algorithm is the only one which is able to segment all the above mentioned tissues and structures of the neonatal brain. Segmentation accuracy is confirmed by visual evaluations of medical experts, as well as by quantitative comparisons with expert-drawn manual segmentations. The algorithm's robustness is confirmed by tests on images of variable quality, acquired with different machines and protocols, as well as by tests on subjects of varying anatomy (enlarged CSF ventricles, preterm- vs. term-born). In this paper we extend our work previously presented in Gui et al. (2011).

## 2. Method

The proposed segmentation algorithm consists of five steps summarized by the outline in Fig. 1, whose details will be presented in the following sections: extraction of the intracranial cavity and of the two hemispheres, detection of the subcortical gray matter, separation of the cortical gray matter, unmyelinated white matter and CSF, segmentation of the cerebellum and of the brainstem, and detection of the myelinated white matter.

The input data for our algorithm consists of T1 and T2 MR scans of a newborn brain of gestational age (GA) between 38 and 44 weeks. Before segmentation, we apply standard preprocessing steps, similarly to Prastawa et al. (2005) and Weisenfeld and Warfield (2009). Namely, we correct intensity inhomogeneities (bias field) with the method based on image entropy minimization developed by Mangin (2000), implemented in the software BrainVISA (2009). Then, we rigidly register the T2 image to the T1 image based on the mutual information metric (Maes et al., 1997), using the software SPM8 (2009). In order to enable the application

of anatomical knowledge in a consistent manner for all subjects, we align the images according to the radiological orientation (+x – left, +y – anterior, +z – superior). To facilitate image processing with mathematical morphology, we resample the registered T1 and T2 images using cubic spline interpolation (as recommended by Thévenaz et al. (2000)) in order to obtain isotropic voxels. Finally, we apply an anisotropic diffusion filter separately to each of the T1 and T2 images, in order to reduce noise while preserving the edges of brain structures (Perona and Malik, 1990; Gerig et al., 1992).

Before we present the details of our algorithm, we offer a brief description of the watershed segmentation technique, as well as of the gray level morphological opening and closing operations, which are involved in several steps of our algorithm. More details can be found in Beucher and Meyer (1993), Lotufo and Falcão (2000) and Soille (2010).

Conceptually, in watershed segmentation, we regard the input image as a topographic surface where gray level represents the altitude, so that light parts of the image constitute peaks and crests, while dark parts of the image form basins and valleys. Now if we imagine rain falling on this surface and gradually filling the basins and valleys, then the watershed lines are the ridges separating the catchment basins that are created. Therefore, the input function for the watershed segmentation is generally a function whose peaks correspond to the object edges, such as the image gradient. Each catchment basin (watershed region) is associated to a unique regional minima of the image, and in practice the watershed segmentation is obtained via a region growing technique whose seeds are the image regional minima. To avoid over-segmentation, in marker-based watershed the topographical surface is modified by geodesic reconstruction (Lantuejoul and Maisonneuve, 1984) so as to impose the markers as unique regional minima, resulting in a segmentation where the regions correspond one-to-one to the markers. In our algorithm, region markers are obtained automatically based on anatomical knowledge.

Similarly to morphological opening (closing) on binary images, morphological opening (closing) on gray level images removes bright (respectively dark) features of the image whose spatial support is smaller than the structuring element, by bringing them at the gray level of surrounding structures. In terms of surface topology of the gray level image, this is achieved by trimming

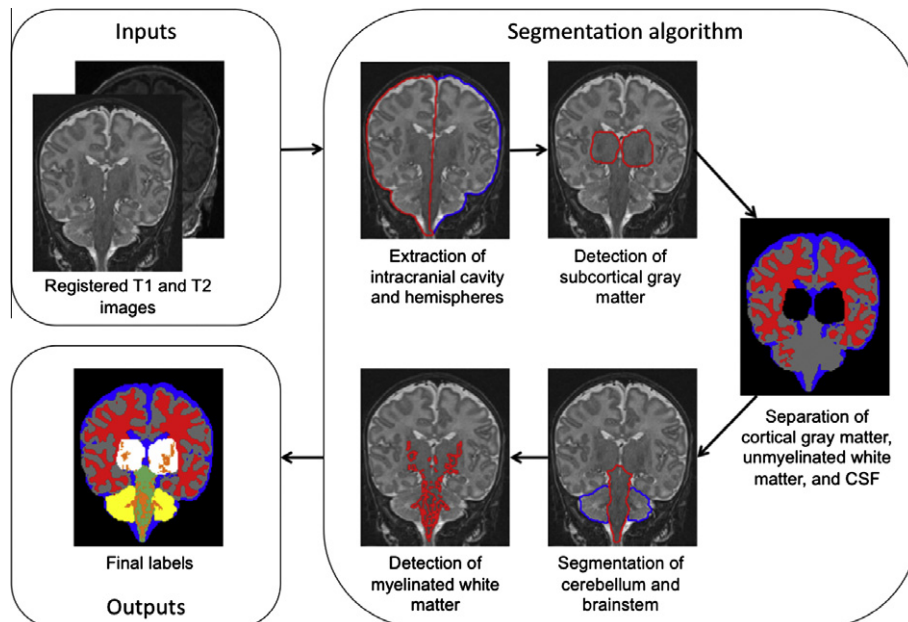


Fig. 1. Outline of the segmentation algorithm.

(respectively filling) the peaks and crests (respectively the basins and valleys) of the surface topology whose spatial support is smaller than the structuring element.

### 2.1. Extraction of the intracranial cavity and separation of the hemispheres

For the extraction of the intracranial cavity (ICC), we use the marker-based watershed algorithm, whose input is given by a segmentation function that we design based on general knowledge about brain morphology. More specifically, we use the knowledge that the ICC is a connected volume, and that its border with the skull is marked by a strong edge on the T2 image. Therefore, we design a watershed segmentation function based on the T2 image gradient. First, we perform an opening of the T2 image, in order to attenuate small hyper-intense regions connected to the ICC (Fig. 2b). Then, we compute the morphological gradient of the opening (Fig. 2c). The segmentation function is constructed by consolidating the gradient, as the sum of increasing scale dilations of the gradient image (Fig. 2d). This method of consolidating the gradient allows us to close any gaps in the gradient image, while maintaining the original edge location. It is based on the observation that the summing of increasing scale dilations of a binary image creates the negative distance map to the white regions of the image (Vachier and Meyer, 2007), thus creating bridges between these regions. This effect is maintained in the case of a gray level image such as ours, thus filling in gaps of the gradient that marks the ICC outline. The morphological operations used to derive the segmentation function are presented in Appendix B1 (Supplementary material of this paper).

The internal and external watershed markers are presented superposed on the segmentation function in Fig. 2d. The internal ICC marker is a small sphere around the gravity center of the head mask, obtained by thresholding the T2 image with the method of Otsu (1979). The external marker is the 3D bounding box of the T2 image. Using these markers and the designed segmentation function, we extract the ICC via watershed segmentation, yielding the contour from Fig. 2e.

The separation of the two hemispheres is based on their symmetry with respect to each other. To determine the inter-hemispheric surface, we employ the same technique of the marker-based watershed, this time using as input a local symmetry function (Fig. 3b), whose maxima mark the inter-hemispheric separation. The advantage of using the watershed segmentation is that it enables us to delineate the 3D surface separating the two hemispheres, rather than being limited to determining the inter-hemispheric plane, like several methods in the literature (Hu and Nowinski, 2003; Volkau et al., 2006). This means that our method can cope with deformations of this surface, as long as the tissues

present local symmetry across the separating surface. In order to quantify this symmetry, we assume that the newborn head is reasonably aligned with the image axes. In our practical experience, this was always the case, since the newborn's position in the scanner is controlled by a technician. The method copes well with small tilts of the head's vertical axis, and if large tilts are present, the head can be easily aligned to the axes via rigid registration with a template.

We derive the symmetry function as the correlation coefficient at each voxel between a small cuboid of the T2 image centered on the voxel and its left–right ( $x$  axis) flip. The dimensions of the cuboid along each axis are set to 20% of the corresponding dimensions of the ICC bounding box. Denoting by  $u$  and  $u'$  the vectorized versions of the two cuboids, the correlation coefficient is

$$\rho_{uu'} = \sigma_{uu'} / \sqrt{\sigma_{uu}\sigma_{u'u'}}, \quad (1)$$

where  $\sigma_{uu'}$  is the covariance of  $u$  and  $u'$ . Since we are only interested in regions with positive correlation coefficients, we obtain the watershed segmentation function by setting the symmetry function to zero in locations with negative correlation coefficients (Fig. 3c). The markers of the two hemispheres (Fig. 3c) are two sagittal planes equally distanced on the  $x$  axis with respect to the ICC gravity center (the inter-plane distance is set to 35% of the ICC width). The contours of the two hemispheres resulted from the watershed segmentation are presented in Fig. 3d.

### 2.2. Detection of the subcortical gray matter

The main difficulty in detecting the subcortical gray matter is given by the fact that it has similar intensity levels with the cortical gray matter. However, it is possible to discriminate the two tissues based on morphological differences. Namely, we exploit the fact that cortical gray matter has a finer structure than the subcortical gray matter, which has a more ‘blobby’ appearance. We use the morphological closing operation on the T2 image in order to lighten the fine dark regions of cortical gray matter, while preserving large dark regions associated with subcortical gray matter. More specifically, we compute the sum of increasing scale closings of the filtered T2 image (Fig. 4b). In the resulted image, the subcortical gray matter can be distinguished as a connected homogenous region, that we determine by means of similarity-based watershed segmentation (Lotufo and Falcão, 2000). The similarity-based watershed is a modification of the classical watershed algorithm, which allows the separation of homogenous regions.

To determine the subcortical gray matter markers for the watershed segmentation, we perform a large scale closing of the T2 image in order to eliminate dark regions corresponding to the cortical gray matter (Fig. 4c). We determine the regional minima

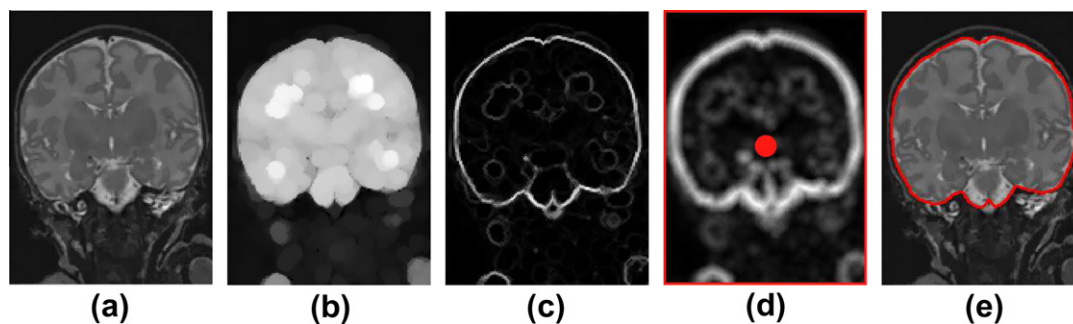


**Fig. 2.** Extraction of the intracranial cavity. Corresponding coronal slices of (a) filtered T2 image; (b) opening of (a); (c) morphological gradient of (b); (d) segmentation function given by the sum of increasing size dilations of the gradient (c), with internal and external markers (in red); (e) watershed segmentation result using the segmentation function and markers from (d). (For interpretation of the references to color in this figure legend, the reader is referred to the web version of this article.)

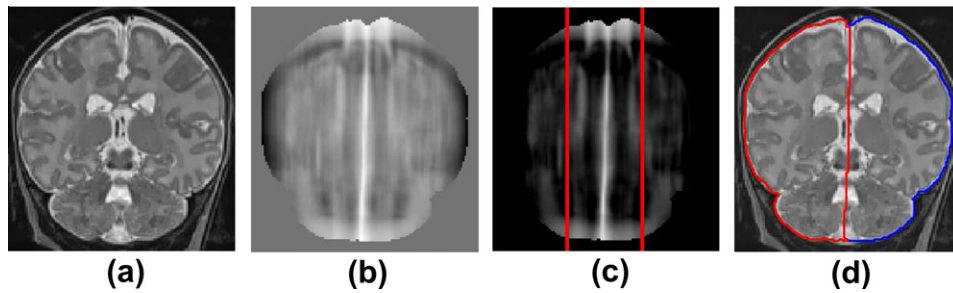


**Fig. 3.** Separation of the two hemispheres. Corresponding coronal slices of (a) filtered T2 image; (b) symmetry function; (c) segmentation function with markers superposed (in red); (d) contours of the two hemispheres resulted from watershed segmentation. (For interpretation of the references to color in this figure legend, the reader is referred to the web version of this article.)

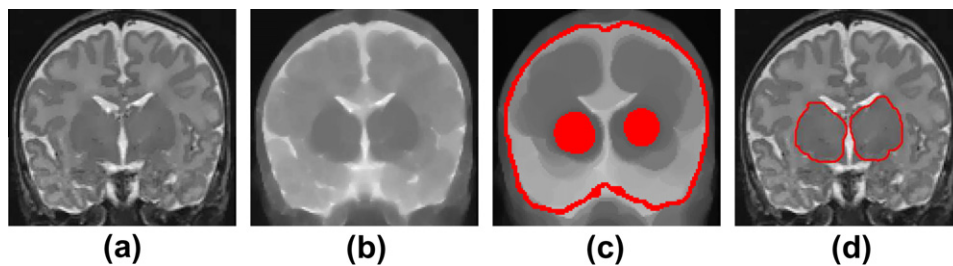


**Fig. 4.** Detection of the subcortical gray matter. Corresponding coronal slices of (a) filtered T2 image; (b) segmentation function given by the sum of increasing scale closings of (a); (c) internal and external watershed markers superposed on large scale closing of the T2 image; (d) contour of the subcortical gray matter resulted from the similarity-based watershed segmentation of (b), using the markers (c).

of this image and, for each hemisphere, we choose as marker the regional minimum which has the highest volume dynamics (as defined in Vachier, 1995; Climent and Sanfeliu, 2006), as presented in Fig. 4c. The external marker is given by the ICC border (Fig. 4c). Starting from these markers and employing the segmentation function given by the sum of T2 image closings (Fig. 4b), we segment the subcortical gray matter via similarity-based watershed, obtaining the result in Fig. 4d. Details of the segmentation function derivation and of the marker selection can be found in Appendix B2 (Supplementary material of this paper).

### 2.3. Detection of the cortical gray matter, of the unmyelinated white matter and of the CSF

One of the challenges of accurately discriminating between the cortical gray matter, the unmyelinated white matter and the CSF is posed by the partial volume effects in the T1 and T2 images, which lead to the misclassification of voxels at the interface between the cortical gray matter and the CSF as unmyelinated white matter. To cope with this problem, we perform segmentation via a region growing method which allows us to impose specific conditions on voxel neighborhood, based on anatomical knowledge.

More specifically, during region growing we discriminate between ventricular CSF and CSF surrounding the cortex (external CSF), enabling us to apply the knowledge that unmyelinated white matter cannot be found in the neighborhood of external CSF. Region growing is limited to the ICC, excluding the subcortical gray matter area previously detected. The algorithm features three regions growing, corresponding to the unmyelinated white matter, the ventricular CSF and the external CSF. The cortical gray matter is obtained as the complement of these regions with respect to the delimited growth area (thus shrinking during the region growing process). To obtain seeds for the three growing regions, we perform  $k$ -means classification (Fig. 5c) of the T2 image values within the growth area in three classes, corresponding to gray matter, unmyelinated white matter and CSF. Then we consider as seeds

regions where the classification is most likely to be correct (Fig. 5d). Namely, we perform an opening of the unmyelinated white matter voxel set and take the largest connected component in each hemisphere as seed for the unmyelinated white matter. Ventricular CSF seeds are given by CSF voxels neighboring subcortical gray matter. External CSF seeds are given by CSF or background voxels (outside the ICC) neighboring the ICC border.

The metric we use for region growing is the Mahalanobis distance (Mahalanobis, 1936) with respect to a set of tissue representative feature vectors:

$$d_M(u, V) = \sqrt{(u - \mu_V)^T \Sigma_V^{-1} (u - \mu_V)}, \quad (2)$$

where the feature vector  $u = (u_1, u_2)^T$  is composed of T1 and T2 image intensities at an image location,  $V$  is a matrix whose columns are the tissue representative feature vectors, and  $\mu_V$  and  $\Sigma_V$  are the mean and covariance, respectively, of the vectors in  $V$ . Representative feature vectors for the gray matter, unmyelinated white matter and CSF (external and ventricular) belong to the corresponding tissue voxels resulted from the  $k$ -means classification.

We start the region growing process from the identified seeds of each tissue class. For each tissue, we select a set of candidate voxels among its unlabeled neighbors, such that their Mahalanobis distance to the tissue is smaller than their Mahalanobis distance to the gray matter tissue class, and they obey a set of neighborhood restrictions. The neighborhood restrictions are used to avoid partial volume errors at tissue interfaces and depend on the tissue type. For the unmyelinated white matter, the eligible candidates exclude external CSF and background voxel neighbors; for the external CSF, they exclude unmyelinated white matter and subcortical gray matter neighbors. Afterwards, we compute the median of the candidates' Mahalanobis distance to their corresponding tissue. We select the tissue of minimum median distance and expand it by including all its eligible candidates whose Mahalanobis distance to the tissue is smaller or equal to the median. Next, we re-compute candidate voxels sets for all tissues and iterate the process until no

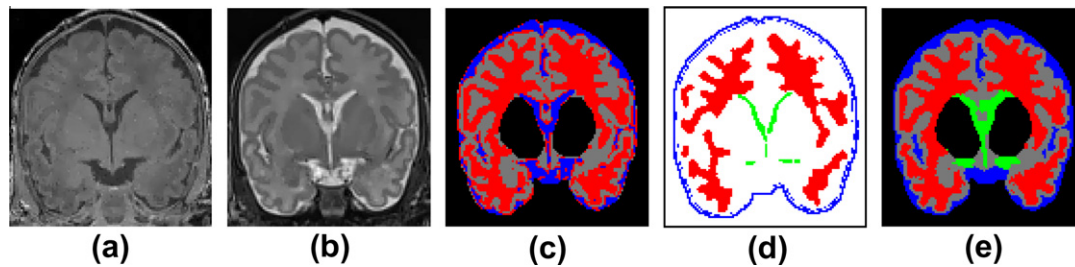


**Fig. 5.** Detection of cortical gray matter, unmyelinated white matter and CSF. Corresponding coronal slices of (a) filtered T1 image; (b) filtered T2 image; (c) result of  $k$ -means classification ( $k = 3$ ) of the T2 image growth region; (d) region seeds (red – unmyelinated white matter, green – ventricular CSF, blue – external CSF); (e) region growing result: gray – cortical gray matter, red – unmyelinated white matter, blue – external CSF, green – ventricular CSF. (For interpretation of the references to color in this figure legend, the reader is referred to the web version of this article.)

voxels can be added to any tissues. The results of the process can be seen in Fig. 5e, showing the classification of the target region into cortical gray matter, unmyelinated white matter, external CSF and ventricular CSF. Notice that the partial volume errors at the CSF/cortex interface affecting the result of the  $k$ -means classification (Fig. 5c) have been eliminated.

#### 2.4. Detection of the cerebellum and of the brainstem

The detection of the cerebellum and of the brainstem is performed in two steps: first the whole cerebellum region is separated from the cerebrum and then it is classified into cerebellum, brainstem and CSF.

##### 2.4.1. Segmentation of the cerebellum region

To separate the cerebellum region, we exploit the knowledge that the cerebellum is surrounded by CSF, and thus there is a fine layer of CSF between the cerebellum and the cerebrum. At the MR image resolution this CSF layer is visible as small pockets of CSF around the cerebellum (Fig. 6a). We reconnect these pockets and emphasize the CSF layer by computing the sum of increasing scale dilations of the unfiltered T2 image, with the ICC background region set to the maximum T2 image intensity (Fig. 6b). In the resulted image, the cerebellum outline is marked by high intensity peaks, thus we can use it as a segmentation function for the marker-based watershed in order to delineate the cerebellum.

To obtain the cerebrum marker, we derive a rough mask of the cerebrum (Fig. 6c, green contour) by dilation and closing of the joint mask of the unmyelinated white matter and subcortical gray matter, previously refined via morphological operations (Fig. 6c, in white). The cerebrum marker is obtained as an erosion of the rough cerebrum mask, to ensure that all its voxels are situated inside the cerebrum region (Fig. 6d, green contour). For the cerebellum marker, we select cortical gray matter voxels not included in the rough

cerebrum mask, and refine the result through morphological operations, followed by erosion, to ensure that all voxels are included in the cerebellum region (Fig. 6d, red contour). Starting from these markers and the segmentation function described above (Fig. 6b), we detect the cerebellum region via watershed segmentation, as illustrated in Fig. 6e. Details of the segmentation function and marker derivation can be found in Appendix B3 (Supplementary material of this paper).

##### 2.4.2. Separation of cerebellum and brainstem

In the following phase, we separate the cerebellum region into cerebellum and brainstem. Both the brainstem and the cerebellum contain a mix of dark (myelin) and light regions of similar intensities, and thus cannot be distinguished based on region homogeneity criteria (Fig. 7a). Our idea is to exploit CSF regions to separate the brainstem from the cerebellum. We create bridges between fragmented CSF regions by computing the sum of dilations of increasing scale of the T2 image, similarly to the previous step (Fig. 7b). Then, we employ the resulted image as a segmentation function for the marker-based watershed, in order to distinguish the brainstem from the cerebellum.

To detect the brainstem and cerebellum markers, we combine intensity information with anatomic landmarks that we detect in the image. Intensity information is introduced via the  $k$ -means classification of the filtered T2 image voxels from the cerebellum region in four classes, denoted, in the order of increasing intensity values, as myelin, gray matter, white matter and CSF. Moreover, we use two anatomic landmarks: the fourth CSF ventricle and a thick inter-hemispheric band. The brainstem is situated anterior to the fourth ventricle and surrounded by cerebellum tissue, while most of the cerebellum is situated posterior to the fourth ventricle (Fig. 7c). Thus, the cerebellum marker will be made of dark voxels (myelin and gray matter) posterior to the fourth ventricle. In the region anterior to the fourth ventricle, the inter-hemispheric band

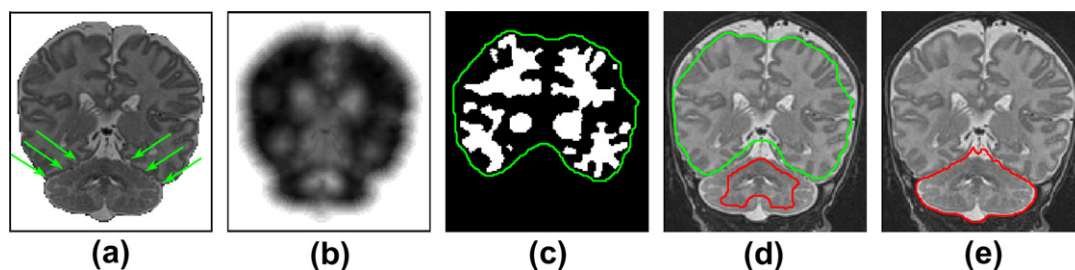


**Fig. 6.** Segmentation of the cerebellum region. Corresponding coronal slices of (a) the unfiltered T2 image (with the ICC background region set to the maximum T2 image intensity); green arrows indicate CSF pockets around the cerebellum; (b) sum of increasing scale dilations of (a); (c) union of unmyelinated white matter and subcortical gray matter sets, refined by opening and largest connected component selection in each hemisphere; (d) watershed markers: cerebrum (green) and cerebellum (red); (e) cerebellum region resulted from watershed segmentation of (b), using the markers (d). (For interpretation of the references to color in this figure legend, the reader is referred to the web version of this article.)

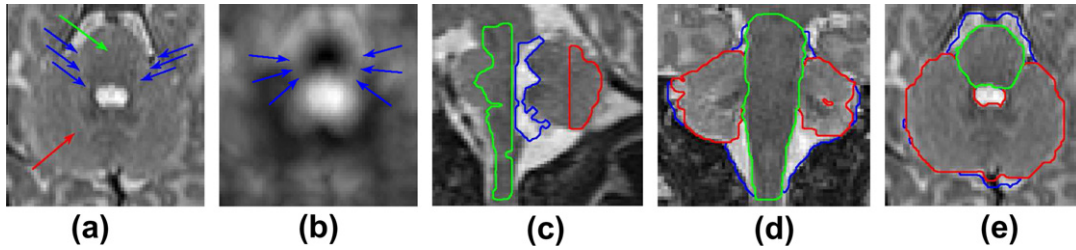


**Fig. 7.** Separation of cerebellum and brainstem. Corresponding axial slices of (a) the unfiltered T2 image (cropped around the cerebellum region), with green arrow indicating the brainstem, red arrow – the cerebellum, and blue arrows – CSF fragments separating cerebellum from brainstem; (b) sum of increasing scale dilations of (a), with blue arrows indicating lighter areas separating cerebellum from brainstem. (c) Sagittal T2 image slice, with contours of brainstem marker (green), cerebellum marker (red), and fourth ventricle CSF (blue). (d) Coronal slice with watershed segmentation result of (b) with the markers (c), refined by CSF removal: brainstem – green contour, cerebellum – red contour, CSF – blue contour. (e) Same as (d), axial slice corresponding to (a,b). (For interpretation of the references to color in this figure legend, the reader is referred to the web version of this article.)

allows us to distinguish dark voxels (myelin) of the brainstem from surrounding cerebellum tissue. The details regarding the segmentation function derivation and the marker detection are presented in Appendix B4 (Supplementary material of this paper).

With the detected markers (Fig. 7c) and the segmentation function described above, we perform marker-based watershed, resulting in a separation of the brainstem and cerebellum regions. These regions are refined by eliminating CSF that was detected in the previous step. The segmented brainstem and cerebellum are presented in Fig. 7d and e.

### 2.5. Detection of the myelinated white matter

To determine myelinated white matter regions within the brain of a newborn from our target age interval (38–44 weeks GA at scan time), we focus the detection on the regions which are most likely to contain myelin at this age (Vasung et al., 2010): the brainstem, the cerebellum and the cortico-spinal tract, which runs through the subcortical gray matter and the periventricular region. Therefore, we define the region where myelin can be found as the union of the subcortical gray matter, the brainstem and the myelinated areas detected in the cerebellum classification (Fig. 8c, blue contour). For the detection we employ 3D region-based active contour segmentation (Chan and Sandberg, 2000; Chan and Vese, 2001), where we introduce a factor constraining the segmentation within the target regions. The inputs of the algorithm are the original non-filtered T1 and T2 images (Fig. 8a and b). Segmentation is achieved by deforming an initial closed surface within the target regions in order to separate myelin from other tissues based on their different mean intensity (lower T2, higher T1).

In practice, we embed the closed surface  $\Gamma \in \mathbb{R}^3$  as the zero level set of a level set function evolving in time  $\phi : \Omega \subset \mathbb{R}^3 \times [0, T) \rightarrow \mathbb{R}$ , which is positive inside the region  $\omega \subset \Omega$  enclosed by the surface  $\Gamma$ , negative outside  $\omega$ , and equals zero on the boundary of  $\omega$  (Osher and Paragios, 2003). We use the signed distance function

to the surface as a level set function, with a positive sign in the interior of the surface and a negative sign in its exterior.

For the segmentation of the myelinated white matter, our separating surface, represented by its embedding level set function  $\phi$ , evolves in order to minimize the following energy:

$$\begin{aligned}
 E(\mu_1^+, \mu_1^-, \mu_2^+, \mu_2^-, \phi) = & \lambda_1 \int \int \int_{\Omega} \left( (f_1(\mathbf{x}) - \mu_1^+)^2 + (f_2(\mathbf{x}) - \mu_2^+)^2 \right) \\
 & \times H_{\epsilon}(\phi(\mathbf{x})) \chi_{\tilde{X}_M}(\mathbf{x}) \, d\mathbf{x} \\
 & + \lambda_2 \int \int \int_{\Omega} \left( (f_1(\mathbf{x}) - \mu_1^-)^2 \right. \\
 & \left. + (f_2(\mathbf{x}) - \mu_2^-)^2 \right) H_{\epsilon}(-\phi(\mathbf{x})) \chi_{\tilde{X}_M}(\mathbf{x}) \, d\mathbf{x} \\
 & + \alpha \int \int \int_{\Omega} |\nabla H_{\epsilon}(\phi(\mathbf{x}))| \chi_{\tilde{X}_M}(\mathbf{x}) \, d\mathbf{x} \\
 & + \beta \int \int \int_{\Omega} H_{\epsilon}(\phi(\mathbf{x})) (1 - \chi_{\tilde{X}_M}(\mathbf{x})) \, d\mathbf{x}. \quad (3)
 \end{aligned}$$

Here  $\lambda_1, \lambda_2, \alpha, \beta \in \mathbb{R}^+$  are fixed positive constants,  $f_1, f_2 : \Omega \rightarrow \mathbb{R}^+$  are the unfiltered T1 and T2 images, respectively,  $\mu_1^+, \mu_1^- \in \mathbb{R}^+$  constitute a piecewise-constant approximation of the image  $f_1$ , corresponding to the regions inside (+) and outside (–) of the segmentation surface, and similarly for  $\mu_2^+, \mu_2^- \in \mathbb{R}^+$  and the image  $f_2$ . The function  $H_{\epsilon} = 0.5 + (1/\pi) \arctan(z/\epsilon)$  is a smooth differentiable approximation of the Heaviside function  $H(z) = \{1 \text{ if } z \geq 0; 0 \text{ if } z < 0\}$ , allowing the discrimination of the two regions  $\omega$  and  $\Omega \setminus \omega$ , which correspond to the positive and, respectively, negative regions of the level set function  $\phi$ . We introduce the function  $\chi_X(\mathbf{x}) = \{1 \text{ if } \mathbf{x} \in X; 0 \text{ otherwise}\}$  as an indicator of the target regions, whose continuous support is denoted in (3) by  $\tilde{X}_M$ . The first two terms of the energy  $E(\mu_1, \mu_2, \phi)$  in (3) impose similarity between the images  $f_1$  and  $f_2$  and their piecewise-constant approximations inside  $(\mu_1^+, \mu_2^+)$  and outside  $(\mu_1^-, \mu_2^-)$  of the segmenting surface. The third term of (3) is a regularization constraint of the segmenting surface, and the last term of (3) limits contour evolution to the

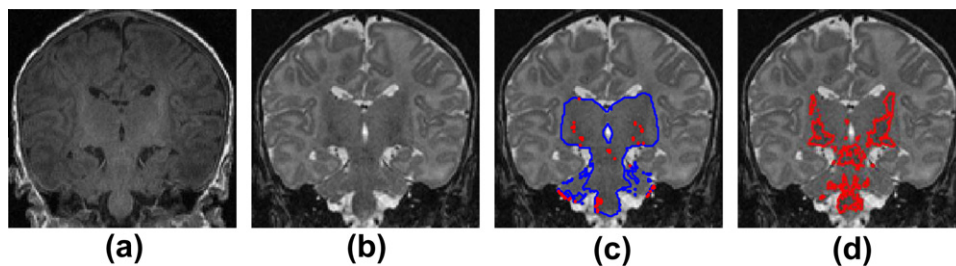


**Fig. 8.** Detection of the myelinated white matter. Corresponding coronal slices of the unfiltered T1 (a) and T2 (b) images; (c) T2 image with contours of the target region for myelin detection (blue) and the segmentation initialization (red); (d) the final myelin region on the T2 image. (For interpretation of the references to color in this figure legend, the reader is referred to the web version of this article.)

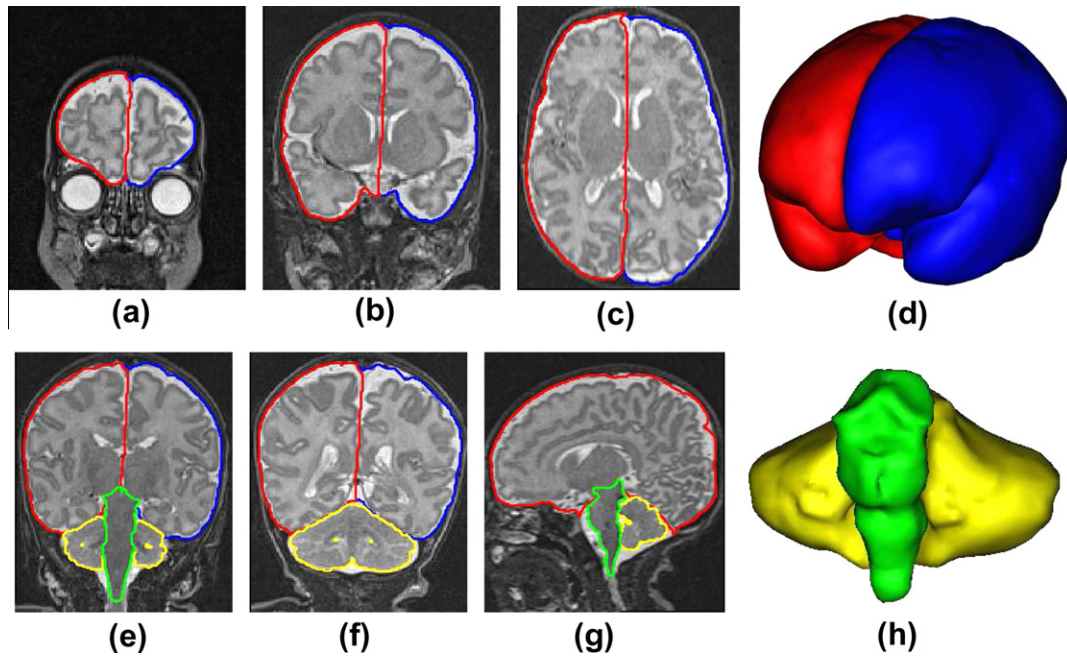


**Fig. 9.** Global scale brain segmentation into the two hemispheres, the brainstem and the cerebellum. Coronal (a, b, e, and f), axial (c) and sagittal (g) T2 image slices with contours of the two hemispheres (red and blue), the brainstem (green) and the cerebellum (yellow); (d) 3D representation of the two hemispheres; (h) 3D representation of the cerebellum (yellow) and brainstem (green). (For interpretation of the references to color in this figure legend, the reader is referred to the web version of this article.)

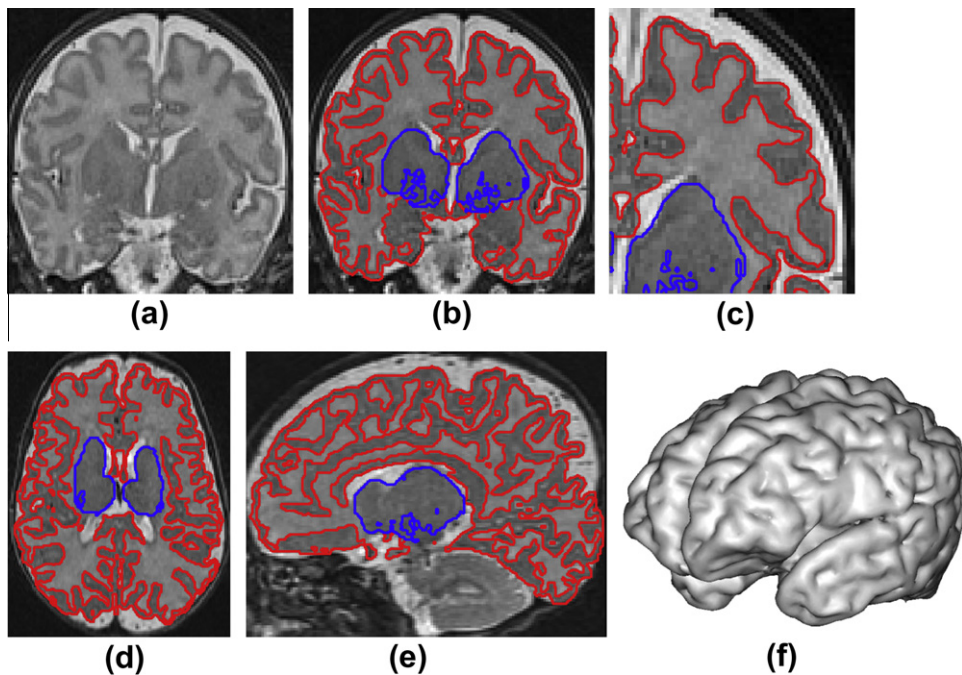


**Fig. 10.** Segmentation of the cortical and subcortical gray matter regions. Corresponding coronal slices of (a) T2 image; (b) T2 image with contours of the cortical gray matter (red) and subcortical gray matter (blue); (c) close-up of the upper right side of (b). Axial (d) and sagittal (e) slices of the T2 image with contours of the cortical gray matter (red) and subcortical gray matter (blue); (f) 3D surface of the cortical gray matter. (For interpretation of the references to color in this figure legend, the reader is referred to the web version of this article.)

target regions  $\tilde{X}_M$ . The minimization of (3) yields the evolution equations for the means  $\mu_1^+$ ,  $\mu_2^+$  and the level set function  $\phi$  (Appendix C, Supplementary material of this paper).

We set  $\lambda_1 = \lambda_2 = 50$ ,  $\alpha = 0.5$ ,  $\beta = 1$ ,  $\epsilon = 0.5$ . The input images  $f_1$  and  $f_2$  are the unfiltered T1 and T2 images, respectively, where the

values inside the ICC are normalized to zero mean and a standard deviation of one. The initial level set function  $\phi(\mathbf{x}, 0)$  is the signed distance function to the contour of the region containing the 2% lowest intensity T2 image voxels within the target region (Fig. 8c, red contour). Then, we run the evolution equations for

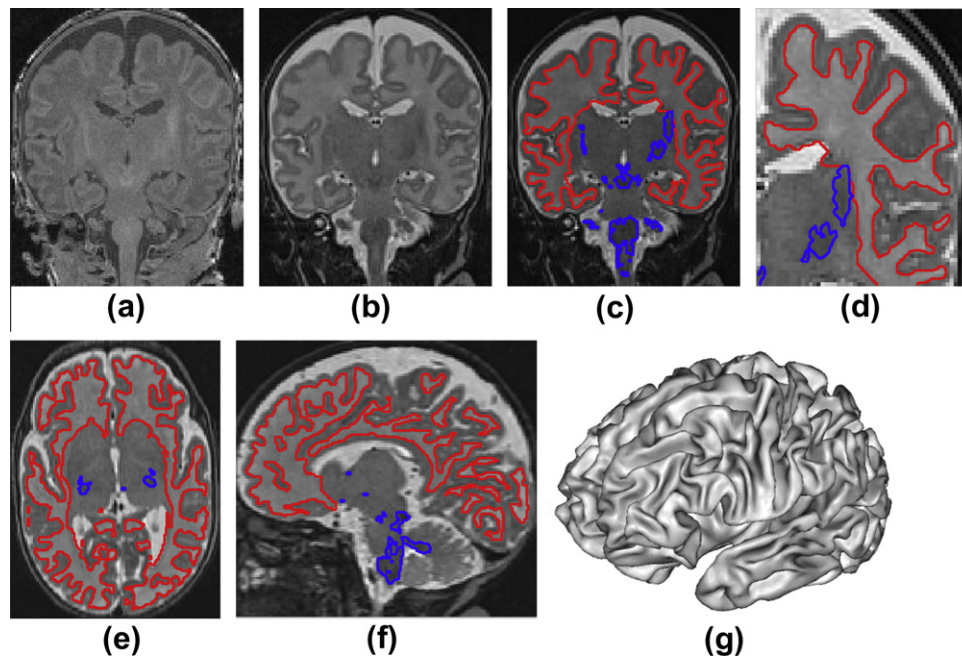


**Fig. 11.** Segmentation of the myelinated and unmyelinated white matter. Corresponding coronal slices of (a) T1 image; (b) T2 image; (c) T2 image with contours of the unmyelinated white matter (red) and myelinated white matter (blue); (d) close-up of the upper right side of (c). Axial (e) and sagittal (f) slices of the T2 image with contours of the unmyelinated white matter (red) and myelinated white matter (blue); (f) 3D surface of the unmyelinated white matter. (For interpretation of the references to color in this figure legend, the reader is referred to the web version of this article.)

the means  $\mu_1^+$ ,  $\mu_2^+$  and the level set function  $\phi$  to convergence. This results in the desired separation of the myelinated white matter regions (Fig. 8d).

### 3. Experimental results and discussion

We tested our segmentation algorithm on 30 healthy newborns with GAs between 38 and 44 weeks, scanned with a Siemens Trio 3T machine. No sedation was used and the images were acquired during the newborns' post-prandial sleep. The infants were fixated with a vacuum pillow and special mini-muffs were applied on their ears to minimize noise exposure. The protocol was approved by the local ethic committee and the infants' parents gave written informed consent for the acquisitions. Coronal images covering the whole head (including the skull) were acquired. For the T1 images, the MPRAGE protocol was used, with TE = 2.5 ms, TI = 1100 ms and TR = 2200 ms. For the T2 image, the TSE protocol was used, with TE = 150 ms and TR = 4600 ms. The resolution for both scans was of  $0.8 \times 0.8 \times 1.2 \text{ mm}^3$ . The acquisition time was of 6 min 29 s for the T1 image, and of 5 min 33 s for the T2 image. Three localizers (axial, coronal and sagittal) were used to ensure proper alignment of the coronal planes with the longitudinal axis of the brainstem. When the acquired images were affected by newborn motion, acquisition was repeated until satisfactory scans could be obtained.

Our algorithm was implemented in MATLAB, using the *SDC Morphology Toolbox for MATLAB* (2008) for the watershed algorithm and morphological operations. All the parameters of the algorithm were fixed to the values indicated in the Appendices, and the segmentation was executed in a fully automated fashion. The algorithm run-time was between 1 h and 1 h 15 min on a 3.06 GHz iMac with an Intel Core 2 Duo processor.

The proposed algorithm segments the newborn brain both globally and at tissue level. At the global level, ours is the first method in the literature that automatically segments the newborn brain into the two hemispheres, the cerebellum and the brainstem, as presented in Fig. 9. At tissue level, the algorithm is able to

accurately capture the fine structure of the cortical gray matter and to correctly distinguish the subcortical gray matter (Fig. 10). Furthermore, the algorithm is robust against misclassifications at tissue interfaces due to partial volume effects. In particular, no voxels at the CSF/gray matter interface are misclassified as unmyelinated white matter, and the unmyelinated white matter is correctly identified, as can be seen in Fig. 11. The resulting tissue surfaces (Figs. 10f and 11g) offer a good representation of the underlying anatomy, with clearly distinguishable gyri and sulci, that can be further analyzed in cortical folding studies (Cachia et al., 2003).

Qualitatively, the segmentations of all subjects were visually inspected by medical experts, who confirmed the good quality of the results. From the quantitative point of view, we examined the level of overlap between our automatic segmentation and manual segmentations drawn by medical experts, on ten subjects. For each subject, a mid-coronal slice containing all the target tissue types was manually segmented by three medical experts. These manual segmentations were used to derive a consensus segmentation via the STAPLE algorithm (Warfield et al., 2004). A visual confirmation of the good agreement between our automatic segmentation and the consensus segmentation is provided by the label images in Figs. 12 and 13. We evaluate this agreement quantitatively by measuring the Dice similarity coefficient between the consensus and the automatic segmentation of the chosen slices:

$$\text{Dice}(A, B) = 2 \frac{|A \cap B|}{|A| + |B|}, \quad (4)$$

where  $A$  and  $B$  are the voxel sets of two different segmentations of a tissue. As can be seen in Table 1, we obtain good agreement between our segmentation and the expert consensus segmentation, as indicated by the Dice coefficient values greater than 0.7 (Zijdenbos et al., 1994). The lowest Dice values (mean  $\pm$  std =  $0.78 \pm 0.04$ ) are obtained for the myelinated white matter, whose detection is a notoriously difficult task, as confirmed by our manual raters and by other authors (Weisenfeld and Warfield, 2009). The difficulty of

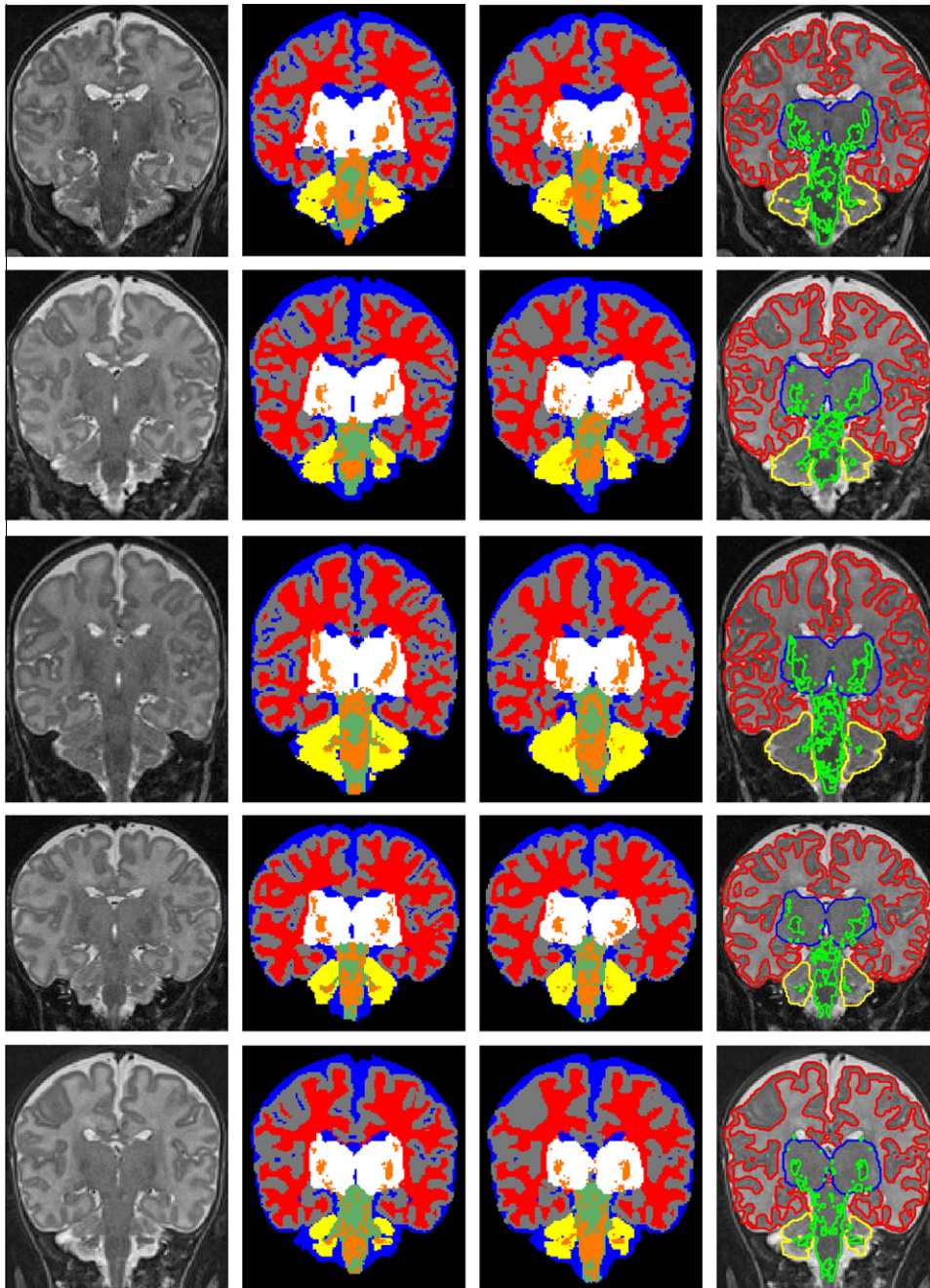


**Fig. 12.** Comparison between the automatic and the expert segmentation. Each row contains: coronal T2 image slices; expert segmentation; automatic segmentation using the T1 and T2 images; corresponding contours of the cortical (red) and subcortical (blue) gray matter, cerebellum (yellow) and myelin (green) on the T2 image. Legend: gray – cortical gray matter, white – subcortical gray matter, red – unmyelinated white matter, orange – myelinated white matter, yellow – cerebellum, green – brainstem (unmyelinated).

distinguishing the fully myelinated white matter regions is due to the fact that the myelination proceeds gradually through the brain, with different regions showing different degrees of myelination. Moreover, myelinated regions have similar intensities to the cortical and subcortical gray matter, to which they are adjacent.

To further assess the reliability of the proposed segmentation method, we compared the Dice coefficient between our segmentation and the expert consensus segmentation with the Dice coefficients between each pair of expert manual segmentations. We report the obtained Dice values averaged for the ten subjects in Table 2. These values show that the differences between the automatic segmentation and the expert consensus are similar to

the inter-expert differences, thus proving that the committed errors are in the same magnitude range as those stemming from inter-expert variability.

The visual comparison of the automatic segmentation results with the experts' consensus segmentation shows small regions of CSF buried in the gyri that were not detected by the automatic segmentation. This is due to the partial volume effect and to the limited spatial resolution, which makes it impossible for the CSF region to enter narrow passages in the cortical gray matter during the region growing process. This limitation does not generate large errors in terms of tissue volumetry, as can be seen from the generally high values of the Dice coefficient. However, we plan to

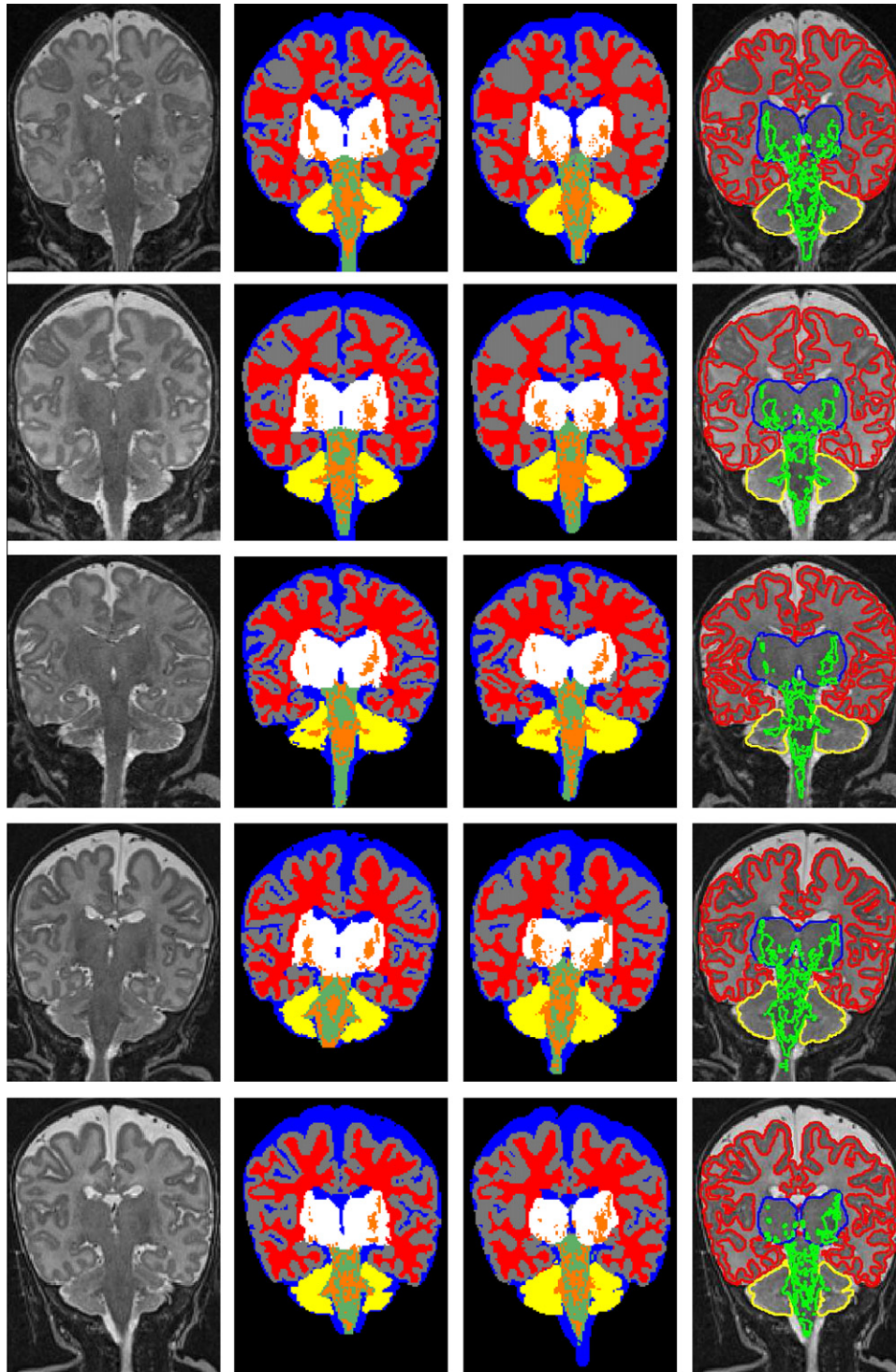


Fig. 13. Comparison between the automatic and the expert segmentation (continued from Fig. 12).

address it in our future work, to enable the straightforward use of the segmentation for an accurate reconstruction of the cortical surface geometry. One direction for improvement would be the use of a dedicated infants' coil for data acquisition, which should allow an increase in image resolution.

Since our method segments additional tissues (such as the cerebellum and the brainstem) compared to other neonatal brain segmentation methods in the literature, it is difficult to perform a direct quantitative comparison of our results with the results of

other methods. However, similarly to our paper, most authors evaluate the Dice coefficient between their proposed segmentation and corresponding manual segmentations. The examination of these evaluations reveals that our Dice coefficients for corresponding tissues are similar or superior to those reported in the literature. For example, Xue et al. (2007) obtain Dice coefficients of  $0.758 \pm 0.037$  for the cortical gray matter, and  $0.794 \pm 0.078$  for the white matter. Prastawa et al. (2005) report median Dice coefficient values of 0.78 for the gray matter, 0.69 for the unmyelinated white matter and

**Table 1**

Dice similarity coefficient between the proposed segmentation and the expert consensus segmentation. Last two lines contain the mean and standard deviation of the Dice values for the ten subjects. GM – cortical gray matter, WM – unmyelinated white matter, SGM – subcortical gray matter, MWM – myelinated white matter, Bm – brainstem, Cb – cerebellum, Std – standard deviation.

Subj.	GM	WM	SGM	MWM	Bm	Cb	CSF
1	0.92	0.95	0.88	0.83	0.90	0.89	0.82
2	0.92	0.93	0.96	0.87	0.93	0.90	0.84
3	0.87	0.89	0.89	0.73	0.87	0.86	0.78
4	0.89	0.94	0.86	0.75	0.87	0.85	0.85
5	0.94	0.96	0.92	0.81	0.93	0.74	0.83
6	0.93	0.95	0.86	0.75	0.88	0.92	0.84
7	0.91	0.92	0.87	0.77	0.89	0.93	0.87
8	0.93	0.95	0.91	0.74	0.94	0.85	0.85
9	0.91	0.93	0.82	0.75	0.86	0.85	0.83
10	0.93	0.96	0.86	0.79	0.93	0.88	0.84
Mean	0.92	0.94	0.88	0.78	0.90	0.87	0.84
Std	0.02	0.02	0.04	0.04	0.03	0.05	0.02

**Table 2**

Comparison of the Dice similarity coefficient between the proposed segmentation and the expert consensus segmentation (column 2) with the Dice similarity coefficients between each pair of experts (columns 3–5). The values represent tissue averages for the ten subjects. GM – cortical gray matter, WM – unmyelinated white matter, SGM – subcortical gray matter, MWM – myelinated white matter, Bm – brainstem, Cb – cerebellum.

Tissue	Automatic vs. consensus	Expert 1 vs. Expert 2	Expert 1 vs. Expert 3	Expert 2 vs. Expert 3
GM	0.92	0.89	0.95	0.89
WM	0.94	0.94	0.96	0.94
SGM	0.88	0.89	0.89	0.89
MWM	0.78	0.63	0.67	0.61
Bm	0.90	0.88	0.89	0.89
Cb	0.87	0.86	0.86	0.89
CSF	0.84	0.85	0.89	0.84

0.67 for the myelinated white matter. Wang et al. (2011) obtain Dice coefficient values between 0.85 and 0.9 for the cortical gray matter, white matter and CSF, while Shi et al. (2011a) report Dice coefficients of  $0.89 \pm 0.02$  for the gray matter,  $0.89 \pm 0.01$  for the white matter, and  $0.87 \pm 0.03$  for the CSF.

**Table 3**

Machine and scanning protocol parameters corresponding to the five subjects in Fig. 14. The repetition time (TR), the echo time (TE) and the inversion time (TI) are given in milliseconds, and the flip angle (FA) is given in degrees. The last line of the protocols contains the image resolution.

#	Machine	Field strength	T1 protocol	T2 protocol
1	Siemens Symphony Vision	1.5T	MPRAGE TR = 2200, TE = 4.38 TI = 1100, FA = 9 $1.2 \times 0.93 \times 0.93 \text{ mm}^3$	TSE TR = 6480 TE = 108 $1.2 \times 0.78 \times 0.78 \text{ mm}^3$
2	GE Signa HDx	3.0T	IR-prepped SPGR TR = 5.9, TE = 2.704 TI = 750, FA = 12 $1.4 \times 0.7 \times 0.7 \text{ mm}^3$	FRFSE TR = 4220 TE = 131.4 $1.5 \times 0.7 \times 0.7 \text{ mm}^3$
3	Siemens Avanto	1.5T	MPRAGE TR = 2200, TE = 3.04 TI = 1100, FA = 9 $1.2 \times 0.78 \times 0.78 \text{ mm}^3$	TSE TR = 5700 TE = 151 $1.2 \times 0.78 \times 0.78 \text{ mm}^3$
4	Philips Intera	1.5T	SPGR TR = 12, TE = 4.2024 FA = 25 $1.5 \times 0.7 \times 0.7 \text{ mm}^3$	TSE TR = 4175 TE = 150 $1.5 \times 0.7 \times 0.7 \text{ mm}^3$
5	GE Signa HDx	1.5T	FSPGR TR = 16.792, TE = 7.416 TI = 1100, FA = 25 $1 \times 0.78 \times 0.78 \text{ mm}^3$	FSE TR = 5250 TE = 168.192 $1.2 \times 0.78 \times 0.78 \text{ mm}^3$

To further investigate the robustness of our algorithm, we tested it on images acquired on different machines and using different acquisition protocols and parameters (according to Table 3), which resulted in variable image quality. As presented in Fig. 14, the images are affected by heavy noise (rows 1 and 2), motion artifacts (row 5, green arrows), and present variable contrast (particularly low in the T1 images). Upon visual inspection, the segmentation algorithm yields good results for all the scans, demonstrating its robustness when faced with variable image quality.

Last, but not least, we assessed the applicability of our method to neonates belonging to different populations, subject to anatomical variability. More specifically, we segmented two preterm-born infants exhibiting enlarged CSF ventricles (ventriculomegaly), presented in Fig. 15, first two rows, and two term-born infants with normal CSF ventricles, presented in Fig. 15, last two rows (scans affected by motion, as indicated by green arrows in the sagittal images). The preterm-born infants were scanned at term-equivalent age, and the term-born infants were scanned as soon as possible after birth. As established in the literature (Inder et al., 2005; Kapellou et al., 2006), there are significant differences in brain shape and structure between preterm- and term-born infants. Such differences can be seen in Fig. 15, where the shapes of the preterm-born infants' brains are more elongated than the shapes of the term-born infants' brains. Despite such differences, and despite structural variability induced by the ventriculomegaly, the visual evaluation of our segmentation reflects good results for all four infants, showing that the algorithm can cope with significant anatomical variability.

#### 4. Conclusion

The main contribution of this work is a novel segmentation algorithm for newborn brain MRI, based on high-level knowledge of neonatal brain morphology, i.e., regarding tissue connectivity, structure and relative positions. We synthesize such knowledge and design specific segmentation functions, which we employ within well-established segmentation methods (such as the marker-based watershed and region-based active contours), operating entirely in 3D. Our algorithm does not require any manual intervention, and does not utilize any brain atlas or template. Moreover, it is the first algorithm to distinguish a complete set of

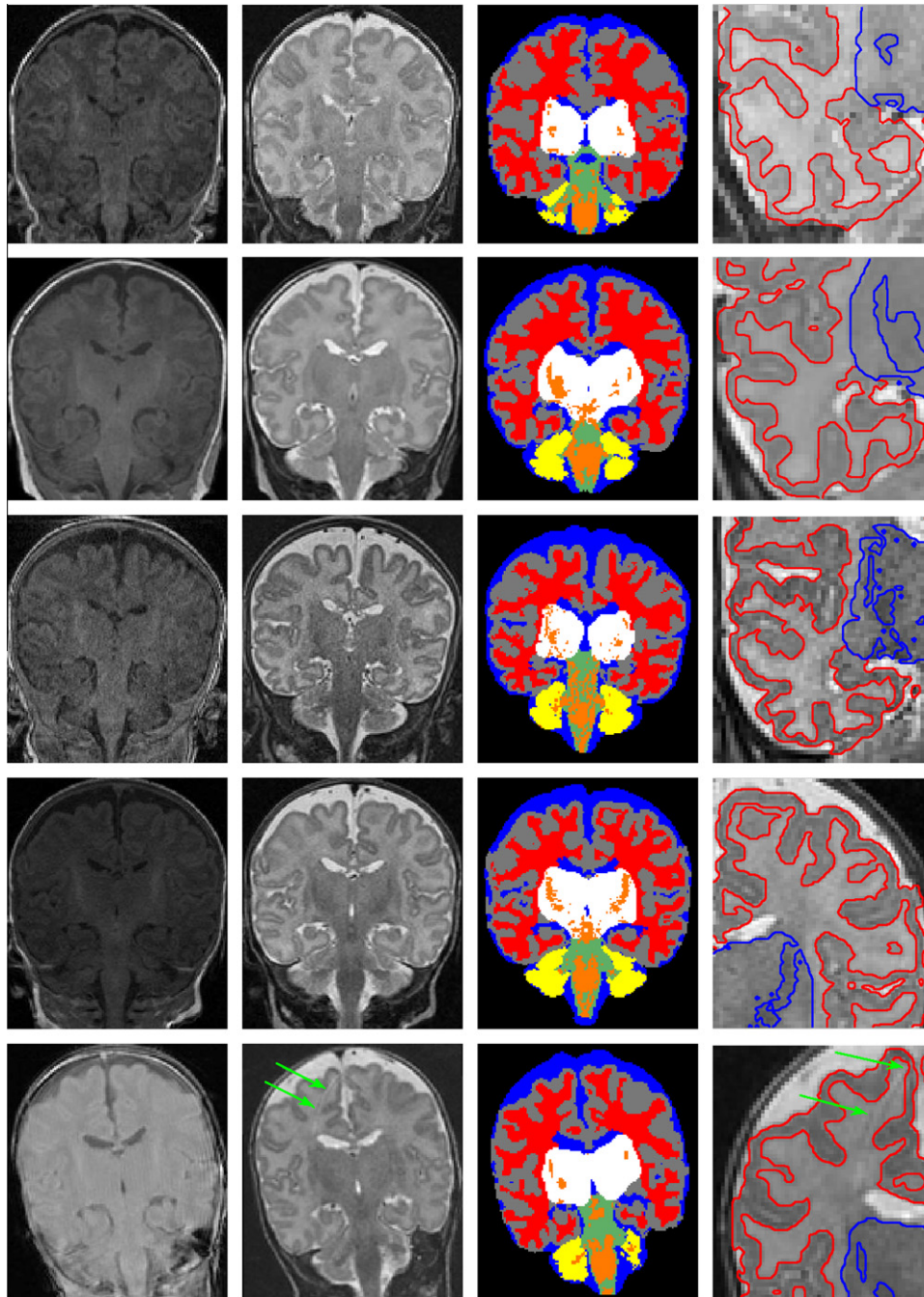


**Fig. 14.** Segmentation of images acquired on different machines, with different protocols (details in Table 3). On each row (left to right): corresponding coronal slices of the T1 image, T2 image, segmentation labels, and magnified portion of T2 image with contours of cortical gray matter (red) and subcortical gray matter (blue). Green arrows in the last row indicate motion artifacts.

brain structures essential for the assessment of brain development at the neonatal age, namely the hemispheres, the cerebellum and the brainstem, cortical and subcortical gray matter, myelinated and unmyelinated white matter and CSF.

The method was successfully tested on 30 healthy infants with GAs between 38 and 44 weeks. The results were visually inspected by medical experts, who reported good overall accuracy of the segmentation for all brain tissues. On a subset of 10 infants, quantitative comparison of the algorithm results with a consensus expert segmentation showed good agreement, with Dice coefficients higher than 0.8 for all tissues except for the myelinated white matter, whose coefficient was higher than 0.7, still indicating good

overlap. The lower scores for the myelinated white matter are due to the gradual nature of the myelination process, and to the intensity similarity between myelinated white matter and cortical and subcortical gray matter, which make it difficult to detect the fully myelinated tissue. Further analysis showed that Dice coefficients between our segmentation and the expert consensus segmentation were similar to Dice coefficients between each pair of expert manual segmentations (three in total), showing that the errors of automatic segmentation are in the same range as those due to inter-expert variability in the case of manual segmentation.

To improve the segmentation of the myelinated white matter, we plan to integrate diffusion images in our future segmentation

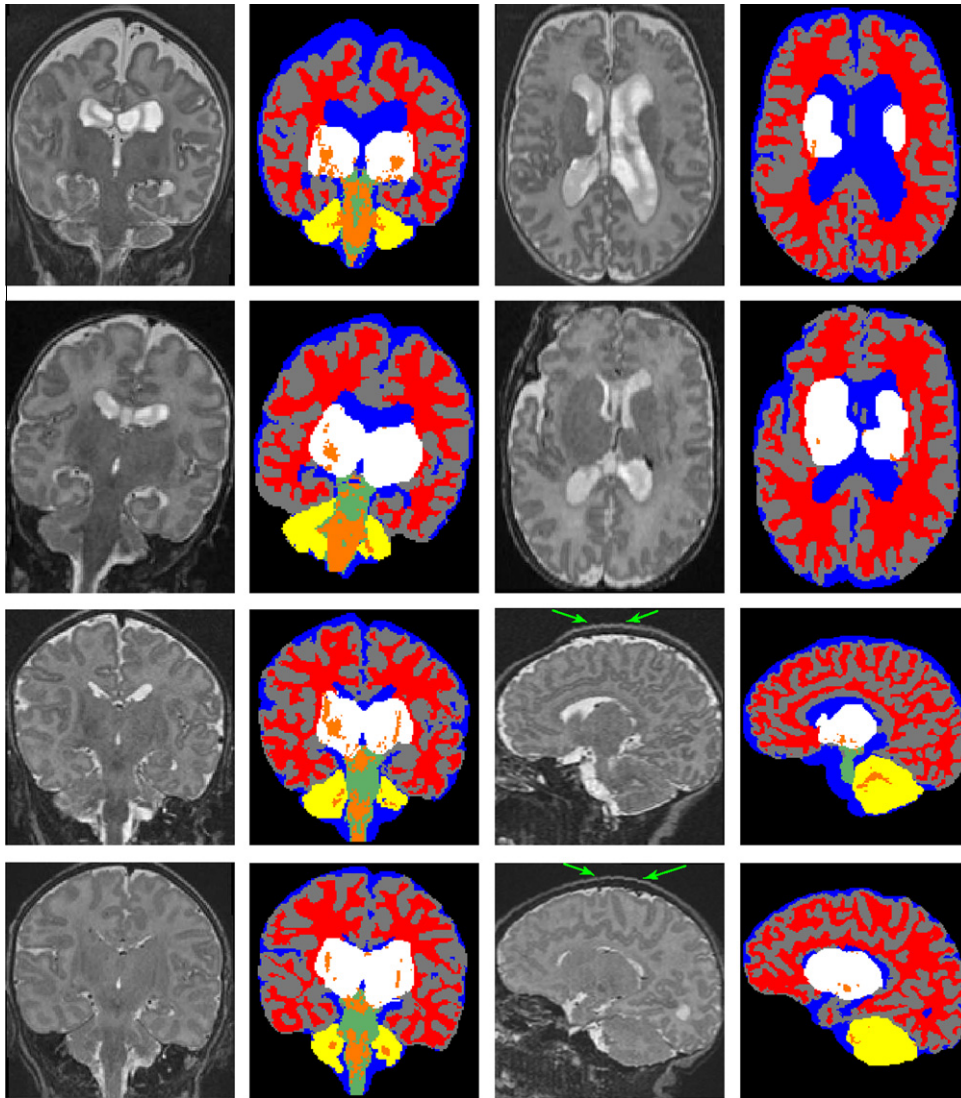


**Fig. 15.** Segmentation of neonatal brain images of variable anatomy. First two rows correspond to two preterm-born neonates exhibiting enlarged CSF ventricles (ventriculomegaly) and contain (left to right): corresponding coronal slices of the T2 image and the segmentation labels, and corresponding axial slices of the T2 image and the segmentation labels. Last two rows correspond to two term-born neonates and contain (left to right): corresponding coronal slices of the T2 image and the segmentation labels, and corresponding sagittal slices of the T2 image and the segmentation labels. Green arrows in the sagittal images indicate coronal slices affected by infant motion.

algorithm. This would enable the precise localization of white matter tracts, which would in turn allow a more precise delineation of the myelinated and unmyelinated white matter, and even a quantification of the myelination degree, in order to better characterize the gradual myelination process.

Further evaluation of our method showed robustness in the segmentation of images of variable quality, acquired with different machines and protocols, and affected by noise, motion and low contrast. Moreover, good results were obtained when testing the method on patients from anatomically-different populations, namely preterm- and term-born neonates, neonates exhibiting enlarged CSF ventricles, as well as neonates with normal CSF ventricles. The applicability of our algorithm to different populations is a direct advantage originating from its design based on general and high-level brain morphology knowledge.

The proposed algorithm performs well for newborns between 38 and 44 weeks GA, and constitutes a solid basis that we plan to extend in order to deal with the segmentation of infant brains from other age intervals of the neonatal period. The extension to younger newborns should be straightforward, since the contrast

between tissues is relatively good. We estimate that the algorithm can also be applied to older infants up to 3 months of age, beyond which it would necessitate major changes in order to deal with the gray matter – white matter contrast inversion.

#### Acknowledgements

This work was supported by the Swiss National Foundation Grants 3200B0-113632 and 33CM30-124101, and by the Center for Biomedical Imaging of the Geneva – Lausanne Universities and University Hospitals and the EPFL. The authors thank Prof. Dimitri Van De Ville for his valuable comments and suggestions that helped improve the quality of this manuscript.

#### Appendix A. Supplementary material

Supplementary data associated with this article can be found, in the online version, at <http://dx.doi.org/10.1016/j.media.2012.07.006>.

## References

- Anbeek, P., Vincken, K.L., Groenendaal, F., Koeman, A., van Osch, M.J.P., van der Grond, J., 2008. Probabilistic brain tissue segmentation in neonatal magnetic resonance imaging. *Pediatr. Res.* 63 (2), 158–163.
- Ashburner, J., Friston, K.J., 2005. Unified segmentation. *NeuroImage* 26, 839–851.
- Bach-Cuadra, M., Schaer, M., André, A., Guibaud, L., Eliez, S., Thiran, J.P., 2009. Brain tissue segmentation of fetal MR images. In: Workshop on Image Analysis for the Developing Brain, 12th International Conference on Medical Image Computing and Computer Assisted Intervention (MICCAI).
- Beucher, S., Meyer, F., 1993. The morphological approach to segmentation: the watershed transformation. In: Dougherty, E.R. (Ed.), *Mathematical Morphology in Image Processing*. CRC Press, New York, pp. 433–481.
- BrainVISA, 2009. <<http://www.brainvisa.info/>>.
- Cachia, A., Mangin, J.F., Rivière, D., Kherif, F., Boddaert, N., Andrade, A., Papadopoulos-Orfanos, D., Poline, J.-B., Bloch, I., Zilbovicius, M., Sonigo, P., Brunelle, F., Régis, J., 2003. A primal sketch of the cortex mean curvature: a morphogenesis based approach to study the variability of the folding patterns. *IEEE Trans. Med. Imag.* 22, 754–765.
- Chan, T., Vese, L., 2001. Active contours without edges. *IEEE Trans. Image Process.* 10 (2), 266–277.
- Chan, T.F., Sandberg, Y.B., 2000. Active contours without edges for vector valued image. *J. Vis. Commun. Image Represent.* 11, 130–141.
- Climent, J., Sanfeliu, A., 2006. Visually significant dynamics for watershed segmentation. In: Proc. 18th International Conference on Pattern Recognition (ICPR'06).
- Cocosco, C.A., Zijdenbos, A.P., Evans, A.C., 2003. A fully automatic and robust brain MRI tissue classification method. *Med. Image Anal.* 7 (4), 513–527.
- Cousty, J., Bertrand, G., Najman, L., Couprie, M., 2010. Watershed cuts: thinnings, shortest path forests, and topological watersheds. *IEEE Trans. Pattern Anal. Mach. Intell.* 32 (5), 925–939.
- Dubois, J., Benders, M., Lazeyras, F., Borradori-Tolsa, C., Leuchter, R.H., Mangin, J.F., Hüppi, P.S., 2010. Structural asymmetries of perisylvian regions in the preterm newborn. *NeuroImage* 52 (1), 32–42.
- Fischl, B., Salat, D.H., Busa, E., Albert, M., Dieterich, M., Haselgrove, C., van der Kouwe, A., Killiany, R., Kennedy, D., Klaveness, S., Montillo, A., Makris, N., Rosen, B., Dale, A.M., 2002. Whole brain segmentation: automated labeling of neuroanatomical structures in the human brain. *Neuron* 33, 341–355.
- Gerig, G., Kübler, O., Kikinis, R., Jolesz, F., 1992. Nonlinear anisotropic filtering of MRI data. *IEE Trans. Med. Imag.* 11 (2), 221–232.
- Grau, V., Mewes, A.U.J., Raya, M.A., Kikinis, R., Warfield, S.K., 2004. Improved watershed transform for medical image segmentation using prior information. *IEEE Trans. Med. Imag.* 23 (4), 447–458.
- Gui, L., Lisowski, R., Faundez, T., Hüppi, P.S., Lazeyras, F., Kocher, M., 2011. Automatic segmentation of newborn brain MRI using mathematical morphology. In: Proceedings of the 8th IEEE International Symposium on Biomedical Imaging: From Nano to Macro (ISBI 2011). pp. 2026–2030.
- Habas, P.A., Kim, K., Rousseau, F., Glenn, O.A., Barkovich, A.J., Studholme, C., 2010. Atlas-based segmentation of developing tissues in the human brain with quantitative validation in young fetuses. *Hum. Brain Mapp.* 31 (9), 1348–1358.
- Hu, Q., Nowinski, W.L., 2003. A rapid algorithm for robust and automatic extraction of the midsagittal plane of the human cerebrum from neuroimages based on local symmetry and outlier removal. *NeuroImage* 20, 2153–2165.
- Hüppi, P.S., Warfield, S.K., Kikinis, R., Barnes, P.D., Zientara, G.P., Jolesz, F.A., Tsuji, M.K., Volpe, J.J., 1998. Quantitative magnetic resonance imaging of brain development in premature and mature newborns. *Ann. Neurol.* 43, 224–235.
- Inder, T.E., Warfield, S.K., Wang, H., Hüppi, P.S., Volpe, J.J., 2005. Abnormal cerebral structure is present at term in premature infants. *Pediatrics* 115 (2), 286–294.
- Kapellou, O., Counsell, S.J., Kennea, N., Dyet, L., Saeed, N., Stark, J., Maalouf, E., Duggan, P., Ajayi-Obe, M., Hajnal, J., Allsop, J.M., Boardman, J., Rutherford, M.A., Cowan, F., Edwards, A.D., 2006. Abnormal cortical development after premature birth shown by altered allometric scaling of brain growth. *PLoS Med.* 3 (8), e265.
- Kuklisova-Murgasova, M., Aljabar, P., Srinivasan, L., Counsell, S.J., Doria, V., Serag, A., Gousias, I.S., Boardman, J.P., Rutherford, M.A., Edwards, A.D., Hajnal, J.V., Rueckert, D., 2011. A dynamic 4D probabilistic atlas of the developing brain. *NeuroImage* 54 (4), 2750–2763.
- Lantuejoul, C., Maisonneuve, F., 1984. Geodesic methods in image analysis. *Pattern Recogn.* 17, 117–187.
- Leemput, K.V., Maes, F., Vandermeulen, D., Suetens, P., 1999b. Automated model-based tissue classification of MR images of the brain. *IEEE Trans. Med. Imag.* 18, 897–908.
- Leroy, F., Mangin, J.F., Rousseau, F., Glasel, H., Hertz-Pannier, L., Dubois, J., Dehaene-Lambertz, G., 2011. Atlas-free surface reconstruction of the cortical grey-white interface in infants. *PLoS One* 6 (11), e27128.
- Lotufo, R., Falcão, A., 2000. The ordered queue and the optimality of the watershed approaches. In: Goutsias, J., Vincent, L.M., Bloomberg, D. (Eds.), *Mathematical Morphology and its Application to Image and Signal Processing*. Kluwer Academic Publishers.
- Maes, F., Collignon, A., Vandermeulen, D., Marchal, G., Suetens, P., 1997. Multimodality image registration by maximization of mutual information. *IEEE Trans. Pattern Anal. Mach. Intell.* 16 (2), 187–198.
- Mahalanobis, P.C., 1936. On the generalised distance in statistics. In: Proceedings of the National Institute of Sciences of India, vol. 2, no. 1, pp. 49–55.
- Mangin, J.F., 2000. Entropy minimization for automatic correction of intensity nonuniformity. In: IEEE Workshop MMBIA. Hilton Head Island, South Carolina, pp. 162–169.
- Oishi, K., Mori, S., Donohue, P.K., Ernst, T., Anderson, L., Buchthal, S., Faria, A., Jiang, H., Li, X., Miller, M.I., van Zijl, P.C.M., Chang, L., 2011. Multi-contrast human neonatal brain atlas: application to normal neonate development analysis. *NeuroImage* 56 (1), 8–20.
- Osher, S., Paragios, N., 2003. *Geometric Level Set Methods in Imaging, Vision and Graphics*. Springer-Verlag.
- Otsu, N., 1979. A threshold selection method from gray-level histograms. *IEEE Trans. Syst. Man Cyber.* 9, 62–66.
- Perona, P., Malik, J., 1990. Scale-space and edge detection using anisotropic diffusion. *IEEE Trans. Pattern Anal. Mach. Intell.* 12 (7).
- Prastawa, M., Gilmore, J.H., Lin, W., Gerig, G., 2005. Automatic segmentation of MR images of the developing newborn brain. *Med. Image Anal.* 9 (5), 457–466.
- SDC Morphology Toolbox for MATLAB, 2008. <<http://www.mmorph.com/>>.
- Shi, F., Fan, Y., Tang, S., Gilmore, J.H., Lin, W., Shen, D., 2010. Neonatal brain image segmentation in longitudinal MRI studies. *NeuroImage* 49, 391–400.
- Shi, F., Shen, D., Yap, P.T., Fan, Y., Cheng, J.Z., An, H., Wald, L.L., Gerig, G., Gilmore, J.H., Lin, W., 2011a. CENTS: cortical enhanced neonatal tissue segmentation. *Hum. Brain Mapp.* 32, 382–396.
- Shi, F., Yap, P.T., Wu, G., Jia, H., Gilmore, J.H., Lin, W., Shen, D., 2011b. Infant brain atlases from neonates to 1- and 2-year-olds. *PLoS ONE* 6 (4), e18746.
- Soille, P., 2010. *Morphological Image Analysis: Principles and Applications*. Springer.
- Song, Z., Awate, S.P., Licht, D.J., Gee, J.C., 2007. Clinical neonatal brain MRI segmentation using adaptive nonparametric data models and intensity-based Markov priors. In: 10th International Conference on Medical Image Computing and Computer Assisted Intervention (MICCAI). Springer-Verlag, pp. 883–890.
- SPM8, 2009. <<http://www.fil.ion.ucl.ac.uk/spm/>>.
- Suri, J.S., Singh, S., Reden, L., 2002. Computer vision and pattern recognition techniques for 2-D and 3-D MR cerebral cortical segmentation (Part I): A state-of-the-art review. *Pattern Anal. Appl.* 5, 46–76.
- Thévenaz, P., Blu, T., Unser, M., 2000. Interpolation revisited. *IEEE Trans. Med. Imag.* 19 (7), 739–758.
- Vachier, C., 1995. *Extraction de Caractéristiques, Segmentation d'Image et Morphologie Mathématique*. Ph.D. Thesis, E.N.S. des Mines de Paris, Paris, France.
- Vachier, C., Meyer, F., 2007. News from viscousland. In: Proceedings of the International Symposium on Mathematical Morphology, pp. 189–200.
- Vasung, L., Huang, H., Jovanov-Milošević, N., Pletikos, M., Mori, S., Kostović, I., 2010. Development of axonal pathways in the human fetal fronto-limbic brain: histochemical characterization and diffusion tensor imaging. *J. Anat.* 217 (4), 400–417.
- I. Volkau, K.B.P., Ananthasubramaniam, A., Aziz, A., Nowinski, W.L., 2006. Extraction of the midsagittal plane from morphological neuroimages using the Kullback-Leibler's measure. *Med. Image Anal.* 10, 863–874.
- Wang, L., Shi, F., Lin, W., Gilmore, J.H., Shen, D., 2011. Automatic segmentation of neonatal images using convex optimization and coupled level sets. *NeuroImage* 58, 805–817.
- Warfield, S.K., Kaus, M., Jolesz, F.A., Kikinis, R., 2000. Adaptive, template moderated, spatially varying statistical classification. *Med. Image Anal.* 4 (1), 43–55.
- Warfield, S.K., Zou, K.H., Wells, W.M., 2004. Simultaneous truth and performance level estimation (STAPLE): an algorithm for the validation of image segmentation. *IEEE Trans. Med. Imag.* 23, 903–921.
- Weisenfeld, N.I., Mewes, A.U.J., Warel, S.K., 2006. Segmentation of newborn brain MRI. In: Proceedings of the 3rd IEEE International Symposium on Biomedical Imaging: From Nano to Macro, vol. 1, pp. 766–769.
- Weisenfeld, N.I., Warfield, S.K., 2009. Automatic segmentation of newborn brain MRI. *NeuroImage* 47, 564–572.
- Xue, H., Srinivasan, L., Jiang, S., Rutherford, M., Edwards, A.D., Rueckert, D., Hajnal, J.V., 2007. Automatic segmentation and reconstruction of the cortex from neonatal MRI. *NeuroImage* 38 (3), 461–477.
- Yu, X., Zhang, Y., Lasky, R.E., Datta, S., Parikh, N.A., Narayana, P.A., 2010. Comprehensive brain MRI segmentation in high risk preterm newborns. *PLoS One* 5 (11), e13874.
- Zijdenbos, A.P., Dawant, B.M., Margolin, R.A., Palmer, A.C., 1994. Morphometric analysis of white matter lesions in MR images: method and validation. *IEEE Trans. Med. Imag.* 13 (4), 716–724.